Nonlinear Electrophoresis of Colloids Controlled by Anisotropic Conductivity and Permittivity of Liquid-Crystalline Electrolyte

Sathyanarayana Paladugu,[1] Christopher Conklin,[2] Jorge Viñals,[2] and Oleg D. Lavrentovich[1,*]

[1]*Liquid Crystal Institute and Chemical Physics Interdisciplinary Program, Kent State University, Kent, Ohio 44242, USA*

[2]*School of Physics and Astronomy, University of Minnesota, Minneapolis, Minnesota 55455, USA*

(Received 22 August 2016; revised manuscript received 28 January 2017; published 30 March 2017)

Liquid-crystal electrolytes enable nonlinear electrophoresis of colloidal particles with velocities proportional to the square of the applied field. We demonstrate that the magnitude and even the polarity of electrophoretic mobility can be controlled by the anisotropic electric conductivity and dielectric permittivity of the liquid crystal. In particular, the reversal of electrophoretic mobility can be triggered either by temperature or composition changes that alter the signs of the conductivity and permittivity anisotropies. Controllable reversal of mobility adds to the list of advantages of anisotropic electrolytes over their isotropic counterparts.

DOI: 10.1103/PhysRevApplied.7.034033

I. INTRODUCTION

Microscale manipulation of colloidal particles and fluids by electric fields is a broad area of active scientific research ranging from fundamental studies of nonequilibrium phenomena [1–4] to the development of practical devices for informational displays, portable diagnostics, sensing, delivery, and sorting [5–7]. It has been demonstrated recently [4,8–10] that when a nematic liquid crystal is used as an electrolyte instead of an isotropic fluid, electrokinetic phenomena acquire qualitatively new characteristics. An important feature of the nematic electrolyte is that the space charge is generated in the medium, at the distortions of molecular orientations, rather than at the interface between the particle and the electrolyte. Space-charge separation occurs in the applied electric field, which drives positive and negative ions to different regions of the deformed liquid crystal thanks to the anisotropic conductivity and dielectric permittivity [8–10]. The electric field then imposes an electrostatic force on the charged clouds, setting the nematic into electrokinetic flows with the velocities growing as the square of the applied field E (one degree of E separates the charges; the other drives the flows) [8–10]. The quadratic dependence means that the electrophoretic and electro-osmotic velocities do not depend on the polarity of the applied electric field. This feature brings an important advantage of the liquid-crystal-enabled electrokinetics (LCEK) over its isotropic linear counterpart since one can use an alternating current (ac) electric field as a driving force to cause a unidirectional persistent motion of particles or of the liquid crystal with a steady displacement that remains nonzero after averaging over the period of the ac field [9,11]. Furthermore, orientational order of the electrolyte allows one to design trajectories of the colloids by patterning the director $\hat{\mathbf{n}}$ that specifies local orientation of the liquid crystal [8,11].

Theoretically, the electrokinetic velocities are expected to depend on the type of director distortions in the liquid crystal and on the anisotropy [8–10]. In this work, we consider one of the simplest realizations of LCEK, namely, a liquid-crystal-enabled electrophoresis of a sphere of a radius R with perpendicular surface anchoring. When placed in a uniformly aligned nematic cell, with the director aligned, say, along the x axis of the Cartesian coordinate system $\hat{\mathbf{n}}_0 = (1, 0, 0)$ (Fig. 1), such a sphere distorts the director around itself because of the finite strength of the surface anchoring. These distortions being radial near the sphere need to match the far-field uniform director $\hat{\mathbf{n}}_0$. The matching is achieved through the introduction of a point defect, the so-called hyperbolic hedgehog that can be located either on the left side or right side of the sphere (Fig. 1) [12]. Once formed, the hyperbolic hedgehog does not change sides since the energy barrier is orders of magnitude higher than the thermal energy. It also does not change sides when the sample is acted upon by electric fields of a modest amplitude used in this work. The overall director structure of the hedgehog-sphere pair is of the dipolar type. We direct the structural dipole $\mathbf{p} = (p, 0, 0)$ from the hedgehog towards the sphere along the x axis [Fig. 1(b)]. When the hedgehog is located on the left-hand side of the sphere, $p > 0$, the experimental mapping of the material flow around the sphere placed in a liquid crystal with zero dielectric anisotropy suggests that the electrophoretic velocity $\mathbf{v} = (v, 0, 0)$ is antiparallel to the direction of dipole, $v < 0$ [9]. Theoretically, the amplitude of the electrophoretic velocity is predicted to be [9]

$$v = \alpha\varepsilon_0\varepsilon_\perp\eta_\parallel^{-1}(\tilde{\varepsilon} - \tilde{\sigma})RE^2, \tag{1}$$

*olavrent@kent.edu

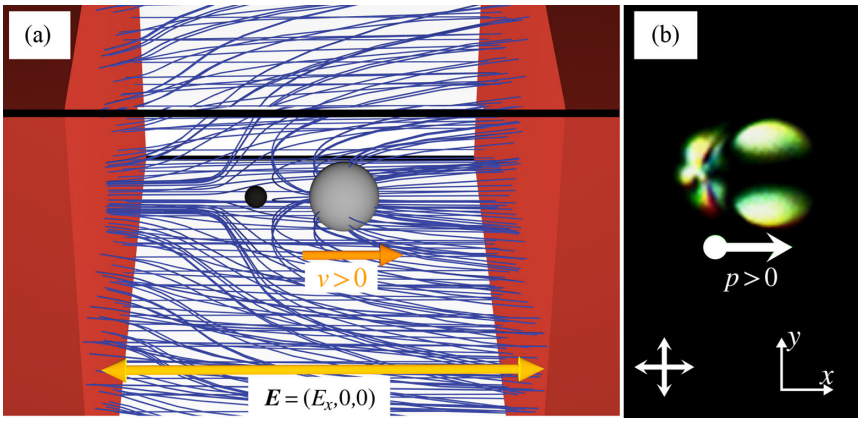

FIG. 1. (a) Scheme of electrophoresis for the case $(\tilde{\varepsilon}-\tilde{\sigma})>0$ and (b) microphotograph of a glass sphere with a point-defect "hedgehog" (located on the left) placed in the nematic liquid crystal seen between cross polarizers. The structural dipole $\mathbf{p}=(p,0,0)$ is shown by an arrow.

where ε_0 is the permittivity in vacuum, $\eta_\parallel$ is the effective nematic viscosity, $\tilde{\varepsilon}=\varepsilon_\parallel/\varepsilon_\perp-1$ is the anisotropic permittivity, and $\tilde{\sigma}=\sigma_\parallel/\sigma_\perp-1$ is the anisotropic conductivity. The subscripts $\parallel$ and $\perp$ refer to the orientation parallel and perpendicular to $\hat{\mathbf{n}}$, respectively, and α is a numerical parameter of the order of 1 that should depend on the details of director configuration, finite surface anchoring, and anisotropic viscoelastic parameters of the nematic. Its exact theoretical value is not known. Although the experiments support the model in the part of $v\propto RE^2$ dependence [8,9,11,13–15] and in the guiding effect of the director field [8,11,16–19], there are no experimental data on how v depends on $\tilde{\varepsilon}$ and $\tilde{\sigma}$, the two crucial properties of the nematic electrolyte. As predicted by Eq. (1), one can reverse the direction of velocity $\mathbf{v}$ with respect to the structural dipole $\mathbf{p}$ by altering the sign of $(\tilde{\varepsilon}-\tilde{\sigma})$. When $(\tilde{\varepsilon}-\tilde{\sigma})>0$, the electrophoretic velocity is parallel to the structural dipole; this case is illustrated in Fig. 1. When $(\tilde{\varepsilon}-\tilde{\sigma})<0$, the two vectors are antiparallel. Flow reversals have been observed in isotropic electrolytes, but their mechanisms are not fully understood [1]. In the present work, we design experiments to verify the key element of the LCEK mechanism by using nematics with broadly varying $\tilde{\varepsilon}$ and values of $(\tilde{\varepsilon}-\tilde{\sigma})$ that reverse their sign as a function of the temperature. We demonstrate that $v\propto(\tilde{\varepsilon}-\tilde{\sigma})$, as predicted by Eq. (1), and can reverse its sign as a function of the composition and temperature.

II. EXPERIMENTAL RESULTS

A. Materials

We use binary mixtures of room-temperature nematics pentylcyanobiphenyl (5CB) and HNG715600-100 (HNG) (purchased from Jiangsu Hecheng Display Technology Co., Ltd.). 5CB exhibits $\tilde{\varepsilon}=1.9$ [20] and HNG exhibits $\tilde{\varepsilon}=-0.7$ [21] at room temperature. The concentration variation of the mixtures changes $(\tilde{\varepsilon}-\tilde{\sigma})$ strongly, both in absolute value and in sign. Dry soda-lime silica spheres of diameter $2R=(9.6\pm1)$ μm (purchased from Thermo Scientific) are used as electrophoretic particles. The spheres are treated with dimethyloctadecyl[3-(trimethoxysilyl) propyl]ammonium chloride to impart perpendicular orientation of $\hat{\mathbf{n}}$. The nematic layers of thickness $h=60$ μm are confined between two glass plates with planar alignment $\hat{\mathbf{n}}_0=(1,0,0)$ achieved by rubbed polymer coating (PI-2555 purchased from HD MicroSystems). The temperature is controlled by a Linkam controller TMS 94 and a hot stage LTS350 (Linkam Scientific Instruments) with accuracy of ±0.01 °C.

B. Electric field distribution in the cell

The ac voltage of frequency $f=25$ Hz and amplitude $U=100$ V is applied between two aluminum strips separated by a distance $L=4$ mm [Figs. 1 and 2(a)]. The electric field at the center of the nematic slab is smaller than the applied field because of the difference in dielectric permittivities of the glass and nematic [9]. The electric field distribution within the cell is determined using the finite-element modeling simulator COMSOL Multiphysics [Fig. 2(b)]. In electric field simulations, we use the following experimental parameters: distance between the electrodes $L=4$ mm, cell thickness $h=60$ μm, dielectric permittivity of glass 3.9, and average dielectric permittivity of the liquid crystal 16. At the center of the cell, the field is uniform; it is parallel to the glass plates, but its amplitude is somewhat smaller than the amplitude of the applied field $E=\beta U/L$, where U is the applied voltage and the correction factor $\beta<1$. For the geometry used in electrophoretic experiments, we find $\beta=0.79$ in the center of the nematic slab [Fig. 2(c)]. Hence, the field acting on the particles in the center of the cells is $E=19.75$ mV/μm which is 79% of the applied field.

C. Reversal of electrophoretic velocity v by composition

We design the experiments in such a way that $\tilde{\varepsilon}$ varies broadly from mixture to mixture, while the anisotropic conductivity remains constant, $\tilde{\sigma}=0.4$. To achieve these conditions, the experiments are performed at the temperature $t=T-T_{NI}=-5$ °C for each mixture, where T_{NI} is the temperature of the isotropic nematic transition of that mixture [Fig. 3(a)]. At high weight concentrations of 5CB,

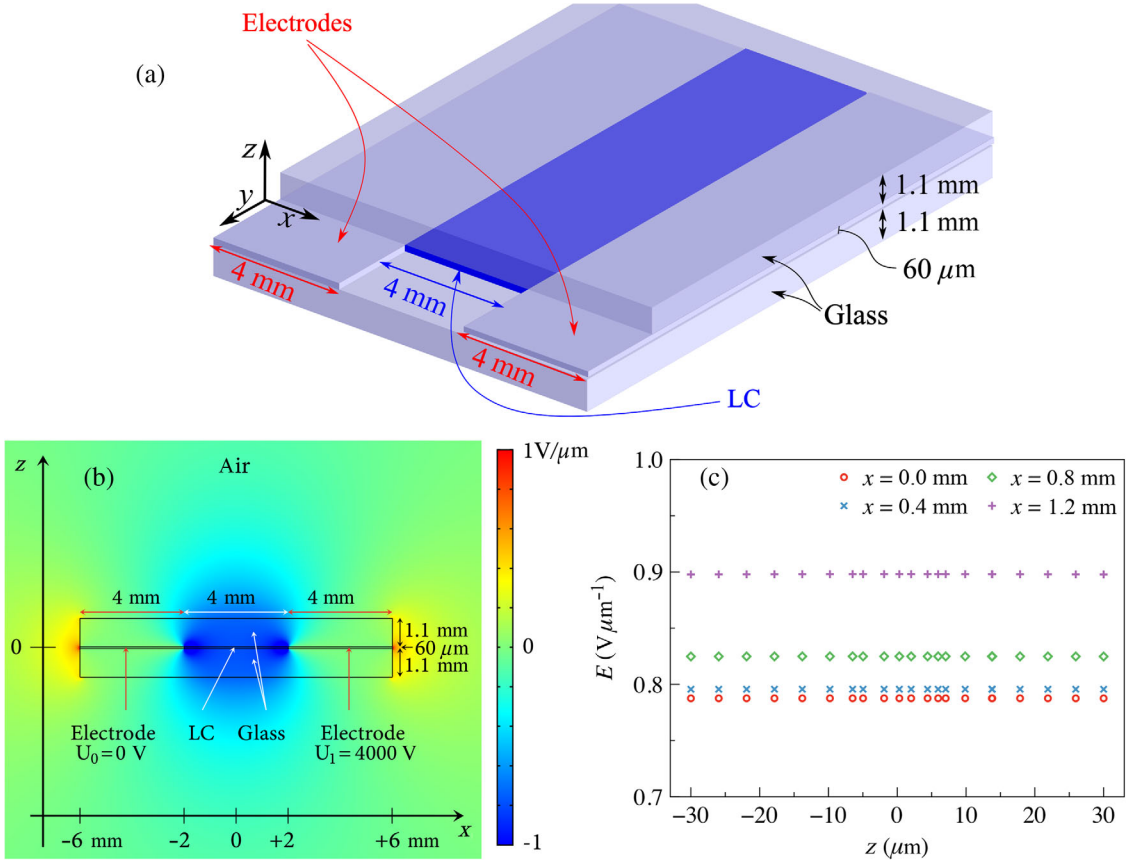

FIG. 2. (a) Schematic diagram of the experimental cell, (b) electric field distribution in the plane of the nematic slab, and (c) electric field at different locations (x, z) within the nematic slab. The point (0,0) corresponds to the geometrical center of the slab.

$c > 0.54$, the spheres move with the sphere leading the way, $v > 0$ [Fig. 3(b)]. For $c < 0.54$, the polarity is reversed, $v < 0$; i.e., the sphere follows the hedgehog [Fig. 3(b)].

D. Reversal of electrophoretic velocity v by temperature change

An analysis of the data in Fig. 3 suggests that the polarity of electrophoresis can be reversed by simply changing the temperature of the nematic mixture with concentrations close to $c = 0.52$. Figure 4 shows that this is indeed the case, as the electrophoretic velocity changes from negative to positive as the temperature decreases, with $t_v \approx -7\,°\mathrm{C}$ being the point of reversal.

To understand the physical reason for the velocity reversal, we perform a thorough characterization of the material properties entering Eq. (1), as described below.

E. Anisotropic electric conductivity

The conductivity of the nematics is of an ionic type [22,23]. Ions are always present in liquid crystals, representing synthetic impurities or being produced at electrodes through dissociation of neutral molecules or absorption from surroundings such as glue, alignment layers, etc. [23]. We measure the concentration using the transient current technique and determine it to be on the order of 10^{20} m^{-3}. To determine $\sigma_\parallel/\sigma_\perp$, we track transient currents in cells of thickness 15 μm with homeotropic and planar alignment, in response to a square wave voltage of frequency 1 Hz and amplitude 4–7 V [24]. The ratio of times required by the ions to migrate through the cell determines the ratio of ionic mobilities, which, in turn, yields $\sigma_\parallel/\sigma_\perp$ and, thus, $\tilde{\sigma}$. We find $\tilde{\sigma} \approx 0.4$ for all mixtures at $t = -5\,°\mathrm{C}$ [Fig. 3(b)].

F. Dielectric anisotropy

The complex dielectric constants $\varepsilon^*(\omega) = \varepsilon'(\omega) - j\varepsilon''(\omega)$, where $j = \sqrt{-1}$, $\varepsilon'(\omega)$, and $\varepsilon''(\omega)$ are the real and imaginary parts of the complex dielectric constants and $\omega = 2\pi f$ is the angular frequency, are measured for a frequency range of $f = 10$ Hz–1 MHz using the Solatron 1260 impedance analyzer and nematic cells with homeotropic and planar alignment. The frequency dependences of the complex dielectric constants are very weak for both alignments. The frequency dependence is fitted using the Cole-Cole equation [25] $\varepsilon^*(\omega) = \varepsilon_\infty + \{(\varepsilon_s - \varepsilon_\infty)/[1 + (j\omega\tau)^{1-\gamma}]\}$, where ε_∞, ε_s are the "infinite frequency" and static dielectric constants, τ is the relaxation time, and γ is an adjustable parameter with a value between 0 and 1. The fitted static dielectric constants obtained for the

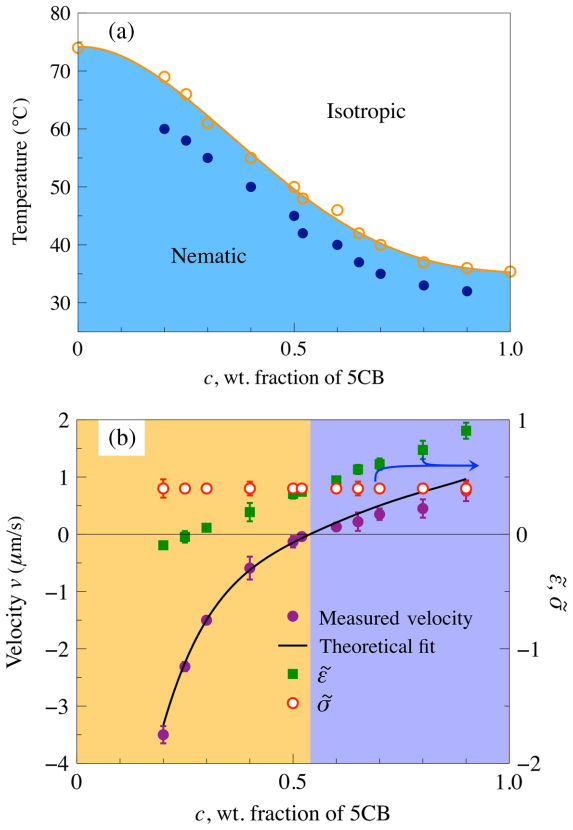

FIG. 3. (a) Phase diagram of 5CB-HNG mixtures. Open circles show T_{NI}, and the filled circles show the temperatures $t = T - T_{NI} = -5\,°C$ at which the material parameters and electrophoretic velocities are measured. (b) Concentration dependence of electrophoretic velocity v, dielectric $\tilde{\varepsilon}$, and conductivity $\tilde{\sigma}$ anisotropies; solid line is the fit of $v(c)$ by Eq. (1) with $\alpha = 1.1 \pm 0.2$.

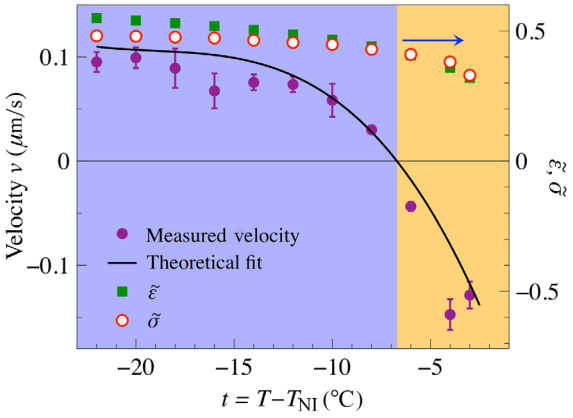

FIG. 4. Temperature-triggered reversal of electrophoretic velocity v plotted together with the temperature dependences of $\tilde{\varepsilon}$ and $\tilde{\sigma}$ for a binary mixture $c = 0.52$; the solid line is the fit of $v(t)$ by Eq. (1), with $\alpha = 1.2 \pm 0.2$.

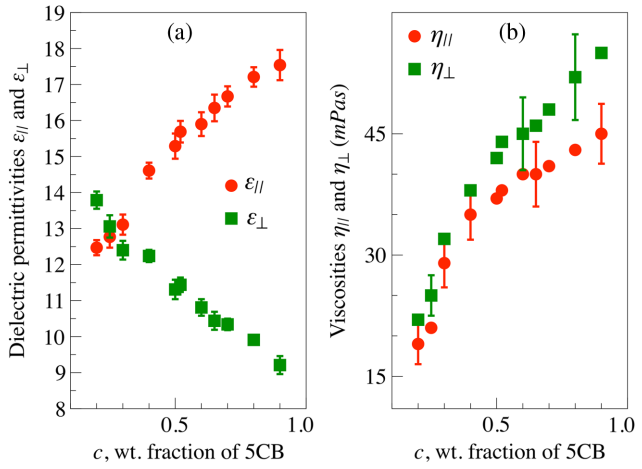

FIG. 5. Concentration dependences of (a) dielectric permittivities and (b) viscosity coefficients measured at $t = -5\,°C$.

homeotropic and planar cell are used as the values of $\varepsilon_\parallel$ and $\varepsilon_\perp$, respectively. Static permittivities $\varepsilon_\parallel$ and $\varepsilon_\perp$ are measured at $t = -5\,°C$ [Fig. 5(a)]. These data are used to plot the function $\tilde{\varepsilon}(c)$ in Fig. 3(b) that crosses $\tilde{\sigma}(c)$ at $c = 0.54$. For the mixture with $c = 0.52$, the dielectric permittivities are measured over the entire range of the nematic phase [Fig. 6(a)]; these data are used to construct the monotonous dependence $\tilde{\varepsilon}(t)$ in Fig. 4.

G. Viscosities

The effective viscosities $\eta_\parallel$ and $\eta_\perp$ [Figs. 5(b) and 6(b)] for the displacements parallel and perpendicular to $\hat{\mathbf{n}}_0$, respectively [26,27], are defined from the generalized Stokes-Einstein equation $\eta_{\parallel,\perp} = k_B T/(6\pi R D_{\parallel,\perp})$ by tracking the Brownian trajectories of the same spheres as those in the electrophoretic experiments. Here, k_B is the Boltzmann constant, T is the absolute temperature, $D_\parallel$ and $D_\perp$ are the two diffusion coefficients measured from the

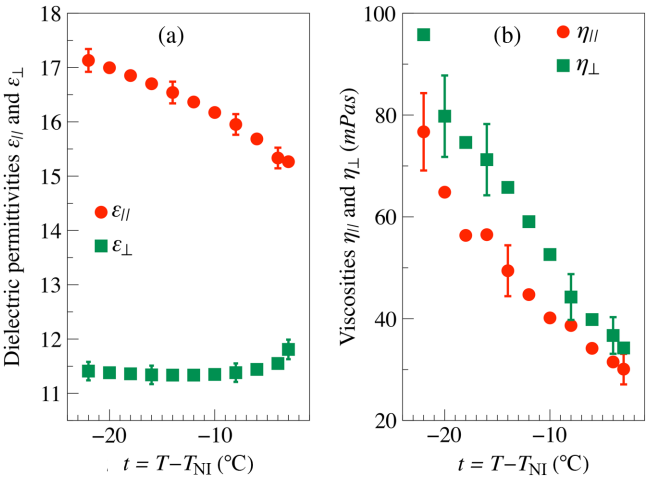

FIG. 6. Temperature dependences of (a) dielectric permittivities and (b) viscosities of the binary mixture at $c = 0.52$.

time dependences of the mean square displacements $\langle \Delta x^2(\tau)\rangle = 2D_{\parallel}\tau$ and $\langle \Delta y^2(\tau)\rangle = 2D_{\perp}\tau$, respectively. The time lag τ is longer than 100 ms to avoid anomalous regimes [28]. Both $\eta_{\parallel}$ and $\eta_{\perp}$ increase with c [Fig. 5(b)]. For the mixture with $c = 0.52$, both $\eta_{\parallel}$ and $\eta_{\perp}$ increase as the temperature is lowered [Fig. 6(b)].

III. DISCUSSION

A. Correlation of velocity reversals and material properties: Experimental data

A comparative analysis of the dependences $\tilde{\varepsilon}(c)$, $\tilde{\varepsilon}(t)$, $\tilde{\sigma}(c)$, $\tilde{\sigma}(t)$, $v(c)$, and $v(t)$ demonstrates a strong correlation between v and the material parameter $(\tilde{\varepsilon} - \tilde{\sigma})$, as predicted by Eq. (1). Namely, v is negative when $(\tilde{\varepsilon} - \tilde{\sigma})$ is negative and positive otherwise [Figs. 3(b) and 4]. Moreover, the experimentally determined $\eta_{\parallel}, \varepsilon_{\perp}, \tilde{\varepsilon}$, and $\tilde{\sigma}$ allow us to fit both $v(c)$ and $v(t)$ dependences with Eq. (1) very well, with the fitting parameter being the same within the experimental error, $\alpha = 1.1 \pm 0.2$ in Fig. 3(b) and $\alpha = 1.2 \pm 0.2$ in Fig. 4.

Equation (1) is deduced in Ref. [9] without an explicit consideration of the exact director configuration caused by the surface anchoring at the surface of the spheres and director deformations that might be caused by the applied field through dielectric surface polarization and flexoelectric mechanisms [29] and by viscous flow effects [30]. Below, we discuss the relative importance of these distortions.

In the so-called one-constant approximation in which all elastic constants of the liquid crystal are equal to each other and to some average value K, the field-induced realigning torques that rotate the director from the sphere-imposed direction by a small angle $\delta\theta$ can be estimated as $(K/\xi)\delta\theta$ for dielectric realignment and as $e^*E\delta\theta$ for the flexoelectric-surface-polarization effect [29]. Here, K is the average Frank constant, $\xi = \sqrt{4\pi K/\Delta\varepsilon}/|E|$ is the dielectric extrapolation length, and $e^* = e_1 + e_3 \pm P$ where e_1 and e_3 are the flexoelectric coefficients, P is the surface polarization. e^* can be as high as [29] $e^* \sim 10^{-10}$ C/m. For the cited electric fields, $K/\xi \sim 3 \times 10^{-8}$ J/m^2 and $e^*E \sim 2 \times 10^{-6}$ J/m^2. The latter value is not negligibly small when compared to the expected polar anchoring strength $(10^{-6}$–$10^{-4})$ J/m^2 [31–33] that is responsible for the appearance of the hedgehog next to the sphere of a diameter $2R \approx 10$ μm. The Ericksen number in the problem estimated roughly as $Er = 2\eta R v/K$ and characterizing a ratio of the viscous to the elastic stress is of the order of 0.1 (for $\eta = 25$ mPa s as $v = 2$ μm/s). This value cannot be considered vanishingly small, which implies that the flow can somewhat distort the director field around the particles in our experiments. Thus, both the field [29] and flow [30] might modify the director and influence α in Eq. (1). To see a stronger effect of viscous stresses, one can either use larger particles or apply a stronger electric field to increase the electrophoretic velocity. Another potential factor influencing α is the difference in dielectric permittivities of the colloid and the nematic, as it leads to gradients of the local electric field.

B. Correlation of velocity reversals and material properties: Numerical simulations.

In order to examine the correlation between the velocity and material properties, gain further insight into the charge distribution and flow field induced by the applied field, and test the effect of surface anchoring on director deformation, we develop a computational model of the transport equations [34]. We consider a 2D geometry replacing the sphere with a disk and neglect surface polarization and flexoelectric effects. Given the small Ericksen number, we use as input the variational solution for the nematic field around a sphere with homeotropic anchoring [12]; we assume that the director configuration is constant. We then solve for the charge distribution and velocity fields under a uniform and oscillatory ac electric field. The particle, a disk of radius R, is considered as immobilized with a fixed location.

We use the finite-element package COMSOL and consider a square domain with the side of $20R$ and a circular hole of diameter $2R = 9.6$ μm at the center, which represents the particle. We use a triangular computational mesh with 54 732 elements, which is refined near the particle and the hedgehog. We consider a fixed conductivity anisotropy $\tilde{\sigma} = 0.4$ and solve the model for permittivity anisotropies ranging from $\tilde{\varepsilon} = -0.3$ to $\tilde{\varepsilon} = 3$. Other physical parameters are given in Table I. The governing equations are investigated from $t = 0$ to $t = 4\pi f$, where f is the frequency of the imposed field. We use no-slip boundary conditions for the velocity field on the edges of both the computational domain and the circular inclusion. The system is closed, so there are no flux boundary conditions for the ionic species. Finally, the electrostatic potential on two opposing boundaries is constant, with a difference given by the magnitude of the imposed field. The potential on the other two boundaries is fixed and linearly interpolates the imposed potential difference. Of course, the potential inside the computational domains follows from the solution of Poisson's equation given the time-dependent charge distribution.

TABLE I. Parameters used in simulations of the liquid-crystal-enabled electrokinetic flows.

Parameter	Value	Description
$\bar{\mu}$	1.45×10^{-9} m^2/(Vs)	Average ion mobility
$\bar{\varepsilon}$	14	Average permittivity
E_0	19.75 mV/μm	Electric field magnitude
f	25 Hz	Frequency of applied field
n_0	10^{19} m^{-3}	Average ion concentration
α_1	−29 mPa s	Leslie-Ericksen viscosity
α_2	−173 mPa s	Leslie-Ericksen viscosity
α_3	−30 mPa s	Leslie-Ericksen viscosity
α_4	118 mPa s	Leslie-Ericksen viscosity
α_5	137 mPa s	Leslie-Ericksen viscosity

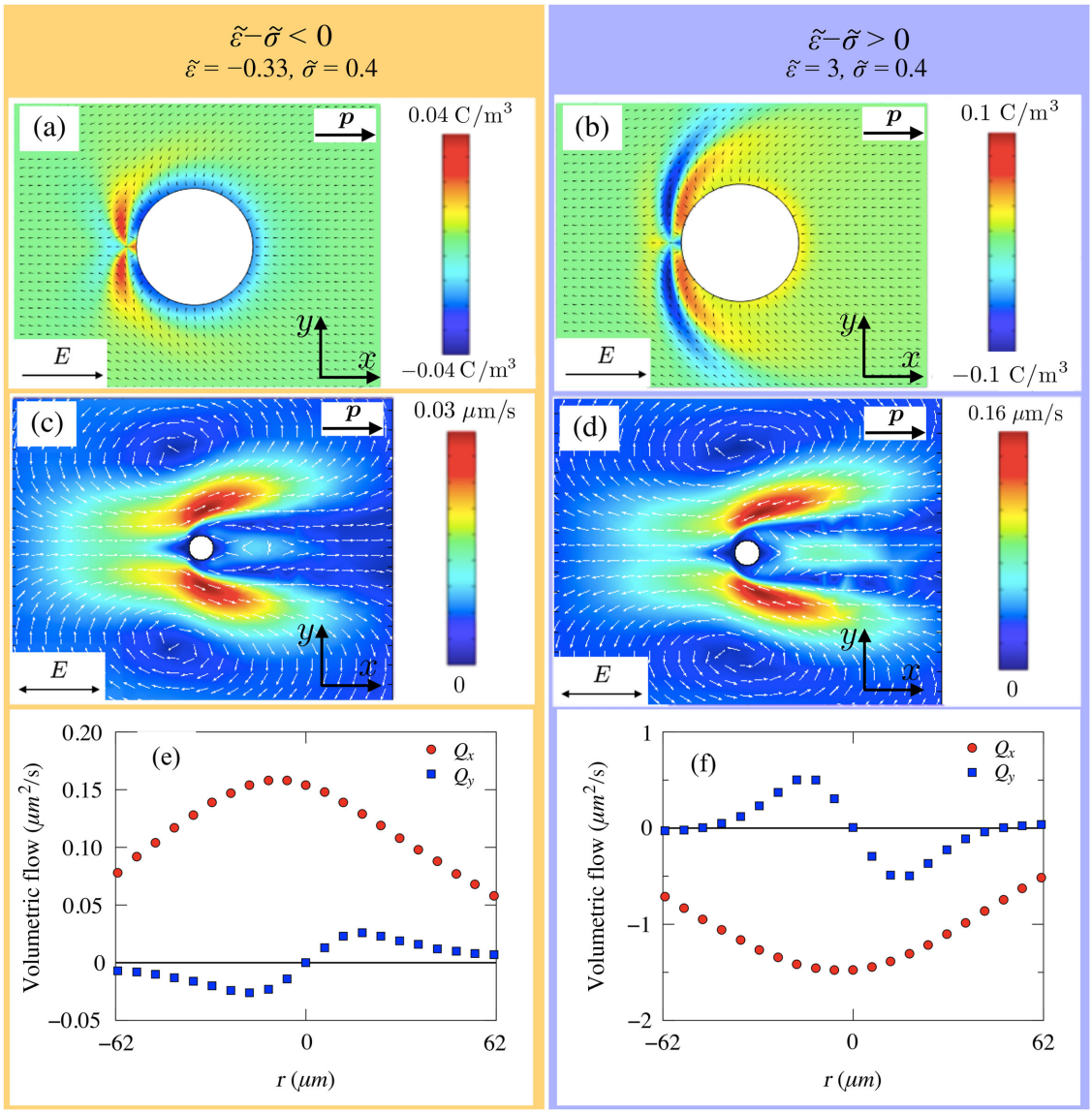

FIG. 7. Numerical solutions for LCEK flows around the fixed particle in two dimensions for various dielectric anisotropies, with applied field parallel to the dipole. (a),(b) Charge density plotted in color, with arrows representing the director field. (c),(d) Corresponding flow velocity map showing flow reversal as $(\tilde{\varepsilon}-\tilde{\sigma})$ changes sign. (e),(f) Volumetric flows along the x axis (Q_x) and along the y axis (Q_y) pumped around the particle by the electric field.

Figure 7 shows the instantaneous charge distribution when $(\tilde{\varepsilon}-\tilde{\sigma})$ is negative [Fig. 7(a)] and positive [Fig. 7(b)] and the corresponding flow fields (averaged over a period of the field) in Figs. 7(c) and 7(d), respectively. Despite the differences in the details, the resulting average flow fields for negative and positive $(\tilde{\varepsilon}-\tilde{\sigma})$ are very similar, except that the flows are completely reversed, as is clear from the comparison of Figs. 7(c) and 7(d) in which the arrows indicate the velocity fields.

The electro-osmotic flows around the particle with the hedgehog defect (Fig. 1) acquire dipolar symmetry due to left-right asymmetry of the dipolar director configuration around the colloid (Fig. 7). The asymmetry in the flows causes pumping of the nematic electrolyte along the x axis, either parallel or antiparallel to the structural dipole $\mathbf{p}$, depending on the sign of $(\tilde{\varepsilon}-\tilde{\sigma})$ [8,9]. In order to determine the net pumping direction near the particle, we compute the volumetric flows along the x axis $Q_x = \int_{-y_0}^{y_0} v_x dy$ and along the y axis $Q_y = \int_{-x_0}^{x_0} v_y dx$, where $x_0 = y_0 = 8R$. Under the action of the electric field, the nematic is pumped from one side of the colloid to another; there is no pumping in the orthogonal y direction [Figs. 7(e) and 7(f)]. An alternative view of this pumping effect can be obtained by computing the viscous force along the x axis on the immobile particle. The average value of this force is by integrating the normal component of the viscous stress over the surface of the particle. The dependence of this average

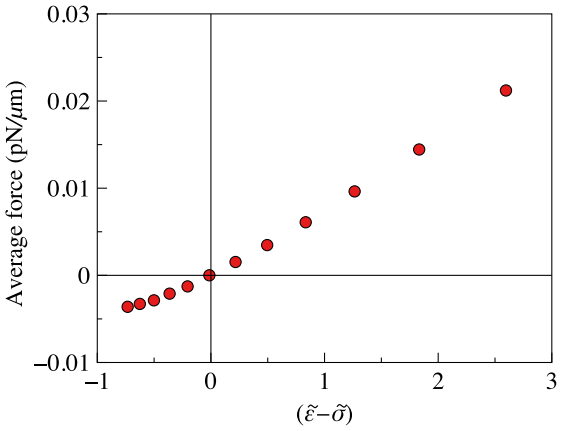

FIG. 8. Average viscous force acting along the x direction on a fixed particle by the LCEK flow calculated for a variety of values of $(\tilde{\varepsilon}-\tilde{\sigma})$ by integrating the normal component of the viscous stress over the particle surface. Since the stress is a force per unit area, the integration yields a force per unit length. The force changes sign with $(\tilde{\varepsilon}-\tilde{\sigma})$.

force on $(\tilde{\varepsilon}-\tilde{\sigma})$ (Fig. 8) shows a reversal of the force direction with the change of the sign of $(\tilde{\varepsilon}-\tilde{\sigma})$. When $(\tilde{\varepsilon}-\tilde{\sigma})<0$, the nematic fluid around the immobilized sphere is pumped along **p** [Fig. 7(e)], and the viscous force on the particle is opposite **p** (Fig. 8). The direction **v** of electrophoretic propulsion of a free particle moving in the nematic with $(\tilde{\varepsilon}-\tilde{\sigma})<0$ should be opposite to the direction of the electro-osmotic pumping in Fig. 7(e) and parallel to the direction of the viscous force calculated in Fig. 8. In the experiment, the free particles in the nematic with $(\tilde{\varepsilon}-\tilde{\sigma})<0$ are indeed moving towards the negative direction of the x axis, $v<0$, with the hedgehog leading the way [Figs. 3(b) and 4]. In other words, the electrophoretic velocity **v** is antiparallel to the dipole **p**. For the case $(\tilde{\varepsilon}-\tilde{\sigma})>0$, the polarity of electroosmotic pumping [Fig. 7(f)] and viscous force [Fig. 8] are reversed. This reversal also implies that the direction of electrophoretic motion [Figs. 1, 3(b), and 4] with respect to the structural dipole should be reversed. As seen in the experiment, when $(\tilde{\varepsilon}-\tilde{\sigma})>0$, the vectors **v** and **p** are parallel to each other; the hyperbolic hedgehog trails the electrophoretically active sphere. Therefore, the numerical simulations confirm the experimentally determined polarity of the electrophoretic motion.

IV. CONCLUSIONS

To summarize, the measured LCEK velocities show a linear dependence on the material parameters of the nematic electrolyte, namely, the dielectric and conductivity anisotropies, as expected from the theory, Eq. (1). The experiments demonstrate that each of these two anisotropies can cause LCEK. Anisotropic conductivity guides the ions along the pathways defined by the director, thus, separating the charges in space. Dielectric anisotropy of a spatially distorted nematic acted upon by the electric field yields a spatially varying local electric field; ions move in response to the nonuniform field pattern, thus, creating the spatial charge. In both cases, the separated charges acted upon by the field that created them result in LCEK flows. Experimentally determined electrophoretic behavior of the free spheres and numerical simulations of the immobilized spheres show a good agreement with each other. In particular, the polarities of the electrophoretic velocities of free particles are opposite to those of the electro-osmotic flows around immobilized particles.

The nematic electrolytes allow one to control both the magnitude and the polarity of electrokinetic flows by simply tuning the temperature or composition to change the value of $(\tilde{\varepsilon}-\tilde{\sigma})$. We determine the numerical coefficient in Eq. (1) that connects the electrophoretic velocity to the material parameters, as $\alpha=1.1$–1.2. An analysis of the experimental data also suggests that the next level of detailed description of LCEK in which α is derived as a function of surface-anchoring strength, flexoelectric and surface-polarization effects, etc., should account for the dynamic nature of the director deformations in the applied electric field and their modification by the flows.

ACKNOWLEDGMENTS

We acknowledge fruitful discussions with M. C. Calderer, D. Golovaty, I. Lazo-Martinez, S. Shiyanovskii, O. M. Tovkach, and N. J. Walkington. We thank J. Xiang for the help in numerical simulations. The work is supported by National Science Foundation Grants No. DMS-1434185 (experiments on electrokinetics), No. DMS-1435372 and the Minnesota Supercomputing Institute (numerical simulations), as well as Grant No. DMR-1410378 (determination of material parameters).

[1] M. Z. Bazant, M. S. Kilic, B. D. Storey, and A. Ajdari, Towards an understanding of induced-charge electrokinetics at large applied voltages in concentrated solutions, Adv. Colloid Interface Sci. **152**, 48 (2009).
[2] I. S. Aranson, Active colloids, Phys. Usp. **56**, 79 (2013).
[3] A. Zöttl and H. Stark, Emergent behavior in active colloids, J. Phys. Condens. Matter **28**, 253001 (2016).
[4] O. D. Lavrentovich, Active colloids in liquid crystals, Curr. Opin. Colloid Interface Sci. **21**, 97 (2016).
[5] J. Dobnikar, A. Snezhko, and A. Yethiraj, Emergent colloidal dynamics in electromagnetic fields, Soft Matter **9**, 3693 (2013).
[6] A. Ramos, *Electrokinetics and Electrohydrodynamics in Microsystems* (Springer-Verlag, Vienna, 2011), p. 530.
[7] M. Z. Bazant and T. M. Squires, Induced-charge electrokinetic phenomena, Curr. Opin. Colloid Interface Sci. **15**, 203 (2010).
[8] C. Peng, Y. Guo, C. Conklin, J. Viñals, S. V. Shiyanovskii, Q.-H. Wei, and O. D. Lavrentovich, Liquid crystals with

patterned molecular orientation as an electrolytic active medium, Phys. Rev. E **92**, 052502 (2015).

[9] I. Lazo, C. Peng, J. Xiang, S. V. Shiyanovskii, and O. D. Lavrentovich, Liquid crystal-enabled electro-osmosis through spatial charge separation in distorted regions as a novel mechanism of electrokinetics, Nat. Commun. **5**, 5033 (2014).

[10] O. M. Tovkach, M. C. Calderer, D. Golovaty, O. Lavrentovich, and N. J. Walkington, Electro-osmosis in nematic liquid crystals, Phys. Rev. E **94**, 012702 (2016).

[11] O. D. Lavrentovich, I. Lazo, and O. P. Pishnyak, Nonlinear electrophoresis of dielectric and metal spheres in a nematic liquid crystal, Nature (London) **467**, 947 (2010).

[12] P. Poulin, H. Stark, T. C. Lubensky, and D. A. Weitz, Novel colloidal interactions in anisotropic fluids, Science **275**, 1770 (1997).

[13] S. Hernàndez-Navarro, P. Tierno, J. Ignés-Mullol, and F. Sagués, AC electrophoresis of microdroplets in anisotropic liquids: Transport, assembling and reaction, Soft Matter **9**, 7999 (2013).

[14] S. Hernàndez-Navarro, P. Tierno, J. Ignés-Mullol, and F. Sagués, Liquid-crystal enabled electrophoresis: Scenarios for driving and reconfigurable assembling of colloids, Eur. Phys. J. Spec. Top. **224**, 1263 (2015).

[15] Y. Nishioka, F. Kobayashi, N. Sakurai, Y. Sasaki, and H. Orihara, Microscopic characterisation of self-assembled colloidal particles in electrohydrodynamic convection of a low-birefringence nematic liquid crystal, Liq. Cryst. **43**, 427 (2016).

[16] I. Lazo and O. D. Lavrentovich, Liquid-crystal-enabled electrophoresis of spheres in a nematic medium with negative dielectric anisotropy, Phil. Trans. R. Soc. A **371**, 20120255 (2013).

[17] Y. Sasaki, H. Hoshikawa, T. Seto, F. Kobayashi, V. S. R. Jampani, S. Herminghaus, C. Bahr, and H. Orihara, Direct visualization of spatiotemporal structure of self-assembled colloidal particles in electrohydrodynamic flow of a nematic liquid crystal, Langmuir **31**, 3815 (2015).

[18] S. Hernàndez-Navarro, P. Tierno, J. A. Farrera, J. Ignés-Mullol, and F. Sagués, Reconfigurable swarms of nematic colloids controlled by photoactivated surface patterns, Angew. Chem., Int. Ed. Engl. **53**, 10696 (2014).

[19] Y. Sasaki, Y. Takikawa, V. S. R. Jampani, H. Hoshikawa, T. Seto, C. Bahr, S. Herminghaus, Y. Hidaka, and H. Orihara, Colloidal caterpillars for cargo transportation, Soft Matter **10**, 8813 (2014).

[20] J. Jadzyn and P. Kêdziora, Anisotropy of static electric permittivity and conductivity in some nematics and smectics A, Mol. Cryst. Liq. Cryst. **145**, 17 (1987).

[21] B.-X. Li, V. Borshch, S. V. Shiyanovskii, S.-B. Liu, and O. D. Lavrentovich, Electro-optic switching of dielectrically negative nematic through nanosecond electric modification of order parameter, Appl. Phys. Lett. **104**, 201105 (2014).

[22] G. Vertogen and W. H. de Jeu, *Thermotropic Liquid Crystals, Fundamentals* (Springer-Verlag, Berlin, 1988).

[23] K. Neyts and F. Beunis, in *Handbook of Liquid Crystals*, edited by J. W. Goodby *et al.* (Wiley-VCH Verlag GmbH & Co., Weinheim, 2014), p. 357.

[24] G. H. Heilmeier and P. M. Heyman, Note on Transient Current Measurements in Liquid Crystals and Related Systems, Phys. Rev. Lett. **18**, 583 (1967).

[25] K. S. Cole and R. H. Cole, Dispersion and absorption in dielectrics I. Alternating current characteristics, J. Chem. Phys. **9**, 341 (1941).

[26] J. C. Loudet, P. Hanusse, and P. Poulin, Stokes drag on a sphere in a nematic liquid crystal, Science **306**, 1525 (2004).

[27] B. Senyuk, D. Glugla, and I. I. Smalyukh, Rotational and translational diffusion of anisotropic gold nanoparticles in liquid crystals controlled by varying surface anchoring, Phys. Rev. E **88**, 062507 (2013).

[28] T. Turiv, I. Lazo, A. Brodin, B. I. Lev, V. Reiffenrath, V. G. Nazarenko, and O. D. Lavrentovich, Effect of collective molecular reorientations on Brownian motion of colloids in nematic liquid crystal, Science **342**, 1351 (2013).

[29] O. D. Lavrentovich, V. G. Nazarenko, V. V. Sergan, and G. Durand, Dielectric quenching of the electric polar surface instability in a nematic liquid crystal, Phys. Rev. A **45**, R6969 (1992).

[30] J.-I. Fukuda, H. Stark, M. Yoneya, and H. Yokoyama, Dynamics of a nematic liquid crystal around a spherical particle, J. Phys. Condens. Matter **16**, S1957 (2004).

[31] Y. A. Nastishin, R. D. Polak, S. V. Shiyanovskii, V. H. Bodnar, and O. D. Lavrentovich, Nematic polar anchoring strength measured by electric field techniques, J. Appl. Phys. **86**, 4199 (1999).

[32] L. M. Blinov, *Structure and Properties of Liquid Crystals* (Springer, Dordrecht Heidelberg London New York, 2011).

[33] T. Rasing and I. Muševič, *Surfaces and Interfaces of Liquid Crystals* (Springer, Berlin, 2004).

[34] C. Conklin and J. Vinals, Electrokinetic flows in liquid crystal thin films with fixed anchoring, Soft Matter **13**, 725 (2017).